

*promoting access to White Rose research papers*



**Universities of Leeds, Sheffield and York**  
**<http://eprints.whiterose.ac.uk/>**

---

This is a copy of the final published version of a paper published via gold open access in **Journal of the American Ceramic Society**

This open access article is distributed under the terms of the Creative Commons Attribution Licence (<http://creativecommons.org/licenses/by/3.0>), which permits unrestricted use, distribution, and reproduction in any medium, provided the original work is properly cited.

White Rose Research Online URL for this paper:

<http://eprints.whiterose.ac.uk/87549>

---

#### **Published paper**

Heath, J.P., Dean, J.S., Harding, J.H. and Sinclair, D.C.J. (2015) *Simulation of impedance spectra for core-shell grain structures using finite element modeling*. *Journal of the American Ceramic Society*, 98 (6). 1925 - 1931.

10.1111/jace.13533

---

# Simulation of Impedance Spectra for Core–Shell Grain Structures Using Finite Element Modeling

James P. Heath, Julian S. Dean,<sup>†</sup> John H. Harding and Derek C. Sinclair

Department of Materials Science & Engineering, University of Sheffield, Sir Robert Hadfield Building, Mappin Street, Sheffield S1 3JD, UK

The volume fraction of core- and shell-regions is an important parameter in the control of temperature-dependent electrical properties of core–shell-microstructured electroceramics such as BaTiO<sub>3</sub>. Here, we highlight the potential unreliability of using capacitance ratios, obtained by simulating impedance spectra, to extract accurate volume fractions of the two regions. Two microstructures were simulated using a finite element approach: an approximation to a core–shell structure (the encased model) and a series-layer model (SLM). The impedance response of the microstructures was simulated for a range of input volume fractions. The volume fractions obtained from the simulation agreed with the input values for the SLM microstructure but differed for the encased model. Current density and electric field plots revealed that this discrepancy was caused by differences between the physical and electrical microstructures of the encased model. A stream trace analysis of current density demonstrated that the current follows the path of least resistance through the core, leaving regions of shell with lower current density. These differences are important when attempting to extract volume fractions from encased microstructures with small cores. In the present case, core volume fractions less than 0.7 produce differences in excess of 25%.

## I. Introduction

IMPEDANCE spectroscopy (IS) is a well-established technique to probe the electrical properties of a wide range of materials<sup>1</sup> and devices.<sup>2</sup> By measuring impedance spectra over a wide-frequency range, it is often possible to identify and characterize electrically distinct regions, for example, bulk and grain-boundary components in electroceramics. To separate different components or processes requires differences in their characteristic relaxation times (or time constants) of at least two orders of magnitude within the measured frequency range.

Ferroelectric BaTiO<sub>3</sub>-based ceramics form the cornerstone of the multilayer ceramic capacitor (MLCC) industry with over 2 trillion units produced each year.<sup>3</sup> Achieving the required  $\pm 15\%$  temperature coefficient of capacitance (TCC) for X7R and X8R<sup>4</sup> capacitors requires control of processing conditions to create electrically heterogeneous grains with a core–shell microstructure. The core regions are undoped-BaTiO<sub>3</sub> (Curie temperature  $\sim 125^\circ\text{C}$ ), whereas the shell (outer) regions contain a distribution of dopants that alter electrical properties (electrical conductivity,  $\sigma$ , and relative permittivity,  $\epsilon_r$ ) and lower the Curie temperature. Jeon *et al*<sup>5</sup> showed that a shell thickness of about a third of the core

radius is needed to obtain satisfactory TCC behavior for (Mg, Y) codoped BaTiO<sub>3</sub> using a combination of transmission and scanning electron microscopy (TEM, SEM) with fixed-frequency dielectric measurements. As BaTiO<sub>3</sub> is sensitive to dopants and contaminants, the core/shell ratio required depends on the dopants and dopant couples used. Moreover, the electrical microstructure may differ from the physical microstructure obtained by measurement of the dopant concentration. Further microstructural characterization is needed to optimize BaTiO<sub>3</sub>-based MLCCs. We have characterized the core and shell volume fractions in commercial positive temperature coefficient of resistance thermistors based on BaTiO<sub>3</sub><sup>6</sup> using IS. Analysis using complex electric modulus plots and spectroscopic plots of the imaginary component,  $M''$ , of the electric modulus suggested that the shell regions were about 20% of the thickness of the core regions. This was confirmed by conductive atomic force microscopy that revealed Schottky barrier regions of  $\sim 500$  nm for an average grain size of  $\sim 5$   $\mu\text{m}$ .<sup>7</sup>

There has been recent interest in the incipient ferroelectric perovskite CaCu<sub>3</sub>Ti<sub>4</sub>O<sub>12</sub> (CCTO) due to the high and temperature stable capacitance behavior of CCTO ceramics at radio frequencies near room temperature. It is now widely accepted that this effect is due to electrical heterogeneity arising from semiconducting grains and insulating grain boundaries for samples processed at  $\sim 1100^\circ\text{C}$ .<sup>8,9</sup> Between the extreme processing conditions of  $700^\circ\text{C}$  and  $1100^\circ\text{C}$ , where insulating and semiconducting grains were clearly revealed by separate peaks in  $M''$  spectroscopic plots, the volume fractions of the two phases were estimated from changes in the  $M''$  peak heights assuming a microstructure with a conductive core and an insulating shell.<sup>10</sup> A similar relationship between volume fractions of Suzuki phases in NaCl, using  $M^*$  arc diameters instead of  $M''$  peak heights, has been reported by Bonanos and Lilley.<sup>11</sup>

These examples show that IS is potentially an easy and reliable technique to quantify core/shell volume fractions but we need to know when it can be employed to characterize the electrical properties of core and shell regions in microstructures. The analyses described above are crude extensions of the brick-work layer model (BLM)<sup>12</sup> used to identify bulk (grain) and grain-boundary responses in electroceramics. In the BLM, an equivalent circuit based on two parallel resistor-capacitor (RC) elements connected in series is used to analyze IS data. One element represents the grain response ( $R_b C_b$ ) and the other represents the grain-boundary response ( $R_{gb} C_{gb}$ ). Both give arcs in complex impedance ( $Z^*$ ) and electric modulus ( $M^*$ ) plots and Debye peaks in  $Z''$  and  $M''$  spectroscopic plots.

The BLM assumes that: all grains are cubic, isotropic and are separated by thin, resistive, regular grain-boundary regions ( $R_{gb} \gg R_b$  and  $C_{gb} \gg C_b$ ); the relative permittivity,  $\epsilon_r$ , of the grain and grain-boundary regions is the same; the time constant,  $\tau = RC$  for the regions differs by at least two orders of magnitude allowing the responses to be resolved in the IS data. The capacitance for each region is a function of

D. J. Green—contributing editor

Manuscript No. 36020. Received December 4, 2014; approved January 28, 2015.

<sup>†</sup>Author to whom correspondence should be addressed. email: j.dean@sheffield.ac.uk

their respective thicknesses for a fixed electrode area and can be calculated from the arc diameters in  $M^*$  plots. The volume ratio of bulk to grain-boundary regions is estimated as the ratio  $C_b/C_{gb}$ .

To test this analysis, we used the BLM of a dual RC circuit to simulate the IS response of grain shell ( $R_1C_1$ ) and grain core ( $R_2C_2$ ) regions, as shown in Fig. 1(a). The resistivity of the shell region is assumed to be three orders of magnitude greater than the core and  $\epsilon_r$  is assumed to be the same for both regions. The volume fraction of the core region,  $\phi_{\text{core}}$ , is estimated from the  $M^*$  arc diameters using the expression<sup>10</sup>:

$$\phi_{\text{core}} = \frac{M'_2}{M'_1 + M'_2} \quad (1)$$

where  $\phi_{\text{core}}$  is the core region volume fraction, and  $M'_1$  and  $M'_2$  are the arc diameters corresponding to the shell and core regions, respectively, as shown in Fig. 1(a). Varying the core-shell volume fraction strongly affects how the current flows through this microstructure. The current must pass through the region of the resistive shell in series with the conductive core region and the electrodes but it may avoid regions of the shell in parallel with the core [see Fig. 1(b)], leading to an inhomogeneous current density within the microstructure. If the shell region in parallel with the core is less electrically active than the core, it will not contribute significantly to the impedance response, giving a discrepancy between the true volume fractions of the regions and those measured using an  $M^*$  plot. Inhomogeneous current density within the microstructure will influence the R and C values extracted for the core and shell regions.

Kidner *et al.*<sup>13</sup> have reviewed a good selection of techniques used to model IS of electroceramics. Some, like effective medium theory (EMT), are analytically solvable.<sup>14</sup> Others, based on Bauerle's BLM,<sup>12</sup> employ large resistor/capacitor networks and require a numerical solution. Here, we compare a conventional BLM analysis for IS data with a finite element model (FEM).

## II. Finite Element Method

We have developed a code<sup>15</sup> that uses Maxwell's equations<sup>16</sup> to solve the electrical response of the system directly for an arbitrary microstructure. The package can consider a full physical microstructure including (but not limited to) grain cores, grain shells, grain boundaries, and electrode contacts. This can include randomized, nonuniform microstructures but we focus here on the validity of extending the BLM

approach to core-shell microstructures. Each region can be assigned material properties independently. This permits all the geometrical and material properties of the physical microstructure to be specified: core-shell volume fractions and their respective  $\sigma$  and  $\epsilon_r$  values. Similar approaches have been used in 2D modeling<sup>17</sup> however, hitherto 3D models have been limited in their complexity.<sup>18</sup>

The simple *physical* microstructures discussed above can be controlled by altering the volume fraction of the core and shell regions. The geometry of the physical microstructure is produced using Voronoi tessellation.<sup>19</sup> First, the required grain shapes are generated. Subgrain features are then produced by shrinking the grain, leaving a volume for the shell region. All regions are then meshed with tetrahedral elements using the program *Gmsh*.<sup>20</sup> The corresponding *electrical* microstructure is determined by analyzing the simulated IS response and comparing with that assumed by the BLM. We assume that both phases have  $\epsilon_r = 100$  and the shell conductivity ( $0.1 \mu\text{S/cm}$ ) is three orders of magnitude lower than the core conductivity ( $100 \mu\text{S/cm}$ ). More realistic scenarios (e.g., noncubic grain microstructures; larger variations in permittivity and conductivity between the components) will be considered in future work.

Two microstructures are considered. The first is Maxwell's series layer model (SLM),<sup>16</sup> consisting of layers of shell and core regions connected in series with the layer normals parallel to the applied voltage difference [Fig. 2(a)]. The second is a core-shell microstructure, shown in Fig. 2(b), consisting of nested cubes where the inner region is the core. This will be referred to as the encased model.

A range of volume fractions for the core region was used for both cases while keeping the material properties constant. The core and shell thicknesses for several core volume fractions (for both models) are listed in Table I. The distance between the electrode contacts was  $2 \mu\text{m}$ . The mesh size was set from a convergence study at 20 000 nodes and over one million elements. The IS response of each model was simulated over the range 1 Hz to 0.1 GHz. At present the model simulates a linear (ohmic) current-voltage relationship. An arbitrary potential difference of 100 V was applied across the model by setting a Dirichlet boundary condition at the top and bottom of the model. All other external surfaces are assigned a Neumann boundary condition to confine the current inside the model. The IS data generated were plotted in  $Z^*$  and  $M^*$  formalisms using the program *Zplot*.<sup>21</sup>

3D representations of the current density, electric field, or electric potential were overlaid on the physical microstructure of the models to facilitate direct comparison. We use the current density distribution to identify regions that contribute significantly to the impedance response. The current density

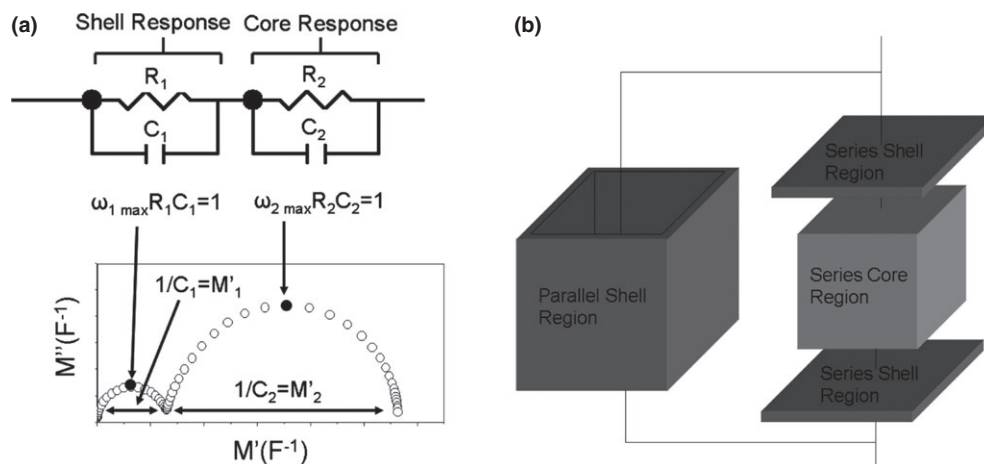
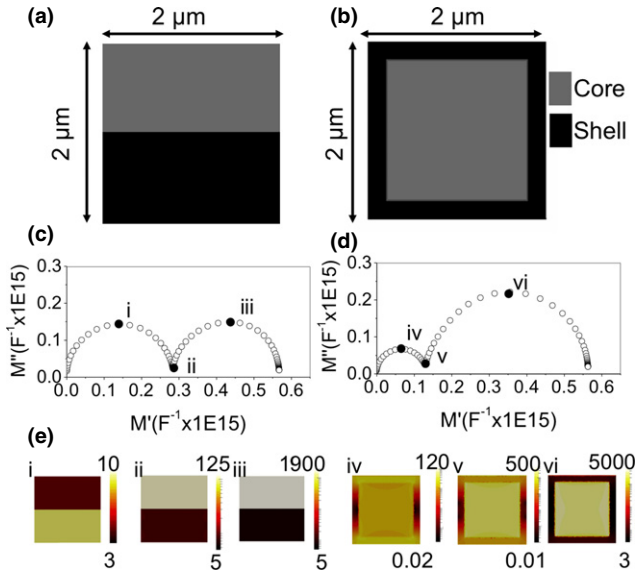


Fig. 1. (a) Schematic of an  $M^*$  plot for a dual RC circuit with intercepts. (b) Schematic of a brick layer representation of a core-shell microstructure.



**Fig. 2.** (a) A schematic of the setup for the SLM and (b) for the encased model for  $V_{\text{core}} = V_{\text{shell}}$ , see Dean *et al*<sup>15</sup> for how this geometry can be modified to form a polycrystal. (c) Simulated IS data are shown as  $M^*$  plots for the SLM and (d) for the encased model. (e) Current density plots are shown for each model at selected frequencies that coincide with  $M''$  inflection points in the  $M^*$  plot for the SLM (i)–(iii) and encased (iv)–(vi) models. All scales are logarithmic and in  $\text{A}/\text{m}^2$ .

plots are taken at frequencies that correspond to the  $M''$  maxima on  $M^*$  plots at the maximum applied voltage. These show the highest concentrations of current density in the shell and core regions (the low and high-frequency  $M''$  maxima, respectively) relative to the rest of the model and permit the electrical microstructure to be compared with the physical microstructure. Electric field plots taken at the same point are used to examine the relationship between electric field and current density.

To analyze the current density plots, the conduction pathways through the model are plotted using a stream trace<sup>22</sup> analysis of the current density vector field produced by the program *ParaView*.<sup>23</sup> This gives the conduction pathway through the model by calculating the curl of the current density. An array of 19 by 19 stream tracer seed points was placed on the bottom electrode surface and the length of each trace measured. The standard deviation of the traces provides the distribution of conduction path lengths (DCPLs).

### III. Results

The impedance response for both the SLM and encased models was simulated for a range of core volume fractions. Output core volume fractions were extracted using Eq. (1)

and the results compared to the input values for both models. The SLM can be solved analytically and the output core volume fraction should be the same as the input value. This was used to validate the FEM code. It is also useful to compare the SLM response, the extracted R, C,  $\tau$  values, and the volume fractions of the core and shell regions with those of the encased model—where current flow will not be homogeneous except for the special cases  $\phi_{\text{core}} = 0$  or 1.

$M^*$  plots of simulated IS data for the SLM and an encased structure (both with equal core and shell phase volume fractions) together with inserted current density plots for various frequencies (i)–(vi) are shown in Fig. 2. The  $M^*$  plots clearly demonstrate that the physical microstructure influences the IS response. For the SLM, the  $M^*$  arc diameters are equal, as predicted for equal volume fractions. However, for the encased model, the shell arc is less than a third of the size of the core arc. Unless the physical microstructure is known, the volume fraction of the core is over-estimated by extracting C from the corresponding  $M^*$  arc (as  $M'$  depends inversely on C). Likewise, the shell volume fraction is underestimated. For the encased model, the current density plots show regions of low current density in the parallel shell regions, as shown in Fig. 2(e) (iv). The current density is homogeneous within the individual core and shell layers for the SLM, as shown in Fig. 2(e) (i)–(iii).

For the SLM, the core volume fraction ( $\phi_{\text{core}}$ ) calculated from the  $M^*$  plots of the simulated IS data was equal to the input value for all volume fractions. For the encased model, the calculated value of  $\phi_{\text{core}}$  was larger than the input value, as shown in Fig. 3(a). The current bypasses the regions of the shell parallel to the core which do not contribute to the  $M^*$  arcs. The Bonanos–Lilley equations<sup>11</sup> describe how a cubic unit of the electrical response of a material modeled by Maxwell’s EMT can be equated to a dual RC circuit and were therefore used to provide an analytical fit to this effect. The agreement between the results obtained from the Bonanos–Lilley equations and the encased model shows that the discrepancies in volume fractions are physically reasonable, as shown in Fig. 3. Although the difference between the input and output core fractions reduces at lower input fractions, expressing the output fraction as a percentage of the input value shows a much higher percentage deviation at smaller values of the input fraction, as shown in Fig. 3(b).

R and C values from  $M^*$  plots were obtained for the core and shell responses using the intercepts and the relationship  $\omega RC = 1$ , see Fig. 1(a). This gave  $\tau$  for the core and shell region of the SLM as 8.67  $\mu\text{s}$  and 8.75 ms, respectively, for all  $\phi_{\text{core}}$ . This agreed with the input material parameters used in the model. For the encased model,  $\tau$  for the shell region ( $\tau_{\text{shell}}$ ) was 8.75 ms for all volume fractions, whereas  $\tau$  for the core region ( $\tau_{\text{core}}$ ) increased with decreasing  $\phi_{\text{core}}$ .  $\tau_{\text{core}}$  (encased model) agreed with  $\tau_{\text{core}}$  (SLM) at  $\phi_{\text{core}} = 1$  but started to increase significantly at  $\phi_{\text{core}} \sim 0.8$  up to  $\sim 5 \tau_{\text{core}}$  (SLM) at  $\phi_{\text{core}} \sim 0.02$ , Fig. 4. Fitting semicircles to the  $M^*$  arcs to calculate  $\tau$  for the core and shell regions revealed

**Table I.** A List of 2D Measurements for the SLM and Encased Model for a Range of  $\phi_{\text{core}}$  or Volume Ratios (3D Measurements)

$\phi_{\text{core}}$ (%)	Volume ratio ( $V_{\text{core}}:V_{\text{shell}}$ )	SLM		Encased	
		Shell thickness ( $\mu\text{m}$ )	Core thickness ( $\mu\text{m}$ )	Shell thickness ( $\mu\text{m}$ )	Core thickness ( $\mu\text{m}$ )
0.02	1:49	1.96	0.04	0.729	0.543
0.1	1:9	1.8	0.2	0.536	0.928
0.2	1:4	1.6	0.4	0.415	1.170
0.5	1:1	1	1	0.206	1.587
0.65	13:7	0.7	1.3	0.134	1.732
0.8	4:1	0.4	1.6	0.072	1.856
0.98	49:1	0.04	1.96	0.007	1.987

$V_{\text{core}}$ , core volume;  $V_{\text{shell}}$ , shell volume.

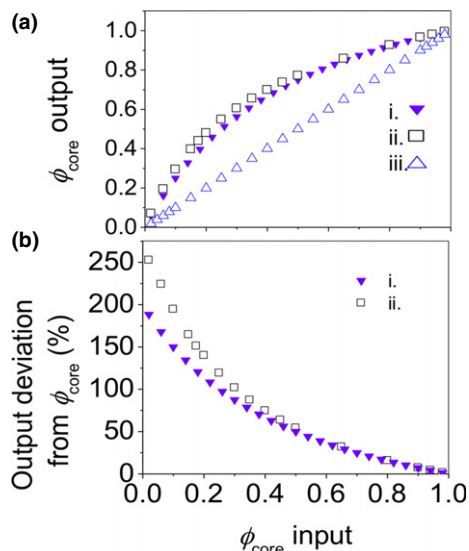


**Fig. 3.** (a) Output volume fraction plotted against input volume fraction for: the Bonanos–Lilley equations (i), the encased model (ii), and the SLM (iii). (b) The percentage deviation in output volume fraction from assigned values plotted against input volume fraction for cases (i) and (ii) above.

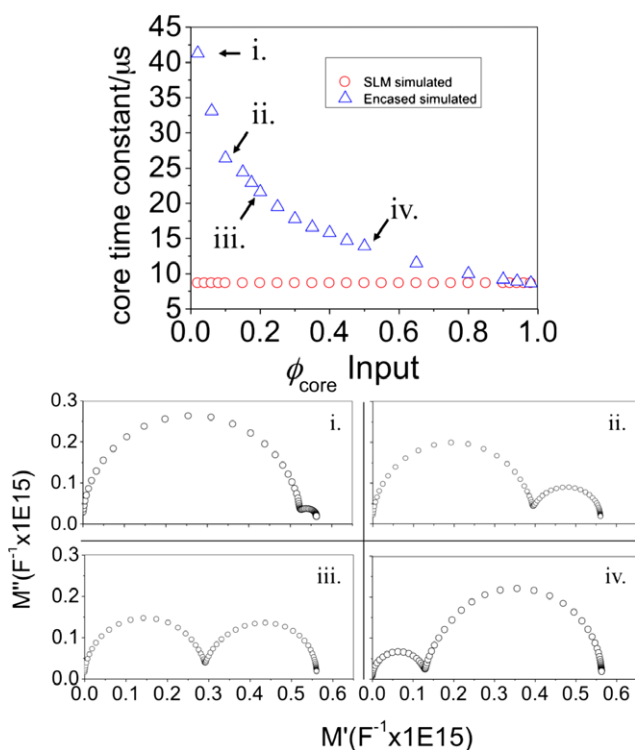


**Fig. 4.** (top) Calculated  $\tau$  values for the core phase obtained from the analysis of  $M^*$  spectra plotted against  $\phi_{\text{core}}$  for the SLM and encased models.  $M^*$  plots (i)–(iv), show an increase in arc merging with decreasing  $\phi_{\text{core}}$ .

more arc merging (greater uncertainty in the  $\tau$  values) at lower values of  $\phi_{\text{core}}$  [see inserted  $M^*$  plots, Fig. 4(i)–(iv)]. The maximum uncertainty was  $\pm 30\%$ , so this alone could not account for the substantial changes in  $\tau_{\text{core}}$  (encased model). The results in Fig. 4 imply a geometrical dependence in the value of  $\tau_{\text{core}}$  (encased model). This contradicts the expectation that  $\tau$  should be geometry independent due to cancellation of the R and C geometric terms.<sup>24</sup>

To further investigate the cause of this geometry-dependent effect, R and C values for the encased model (from the

high-frequency core and low-frequency shell response in  $M^*$  plots) were independently compared to those of the SLM. Except for the special cases  $\phi_{\text{core}} = 1$  and 0, the resistance for the encased shell region ( $R_{\text{shell}}$ ) was lower than  $R_{\text{shell}}$  for the SLM, Fig. 5(a). In contrast, the core resistance ( $R_{\text{core}}$ ) for the encased model was substantially higher than  $R_{\text{core}}$  for the SLM, Fig. 5(b).  $R_{\text{core}}$  for the encased model showed an unusual trend with  $\phi_{\text{core}}$ , Fig. 5(b). There was a linear increase in  $R_{\text{core}}$  from  $\phi_{\text{core}} = 1.0$  down to  $\sim 0.4$ , followed by a leveling-off down to  $\phi_{\text{core}} \sim 0.2$  and finally a steep, nonlinear decrease toward the SLM value at  $\phi_{\text{core}} \sim 0$ . This suggests a transition in the conduction behavior for the model associated with core–shell microstructural effects, especially for  $\phi_{\text{core}} < 0.4$ . Capacitance values for both regions and models had a similar form, increasing as the respective components became thinner. This suggests the enhancement of  $\tau_{\text{core}}$  (encased model) at low  $\phi_{\text{core}}$  is related to conduction pathways through the core phase.

For the encased model, the distribution of conduction path lengths DCPLs at the high-frequency Debye response (for the core region at the frequency associated with the  $M''$  maximum) for a range of input  $\phi_{\text{core}}$  values was obtained using methods described previously. The corresponding current density plots show heterogeneous current flow through the grains with a larger current density in the conductive core. This shows that the current follows the path of least resistance, in good agreement with theory and other computer modeling studies.<sup>15,25,26</sup> When  $\phi_{\text{core}}$  is large, the current flowing through the encased core is almost homogenous but it becomes increasingly heterogeneous as  $\phi_{\text{core}}$  decreases, Fig. 6(a) (i)–(iii). The full-width half maximum (FWHM) value of the  $M''$  peak associated with the encased core response was also measured, as shown in Fig. 6(b). Comparison between the FWHM and values for the DCPLs shows that a broader path length distribution correlates to a broader  $M''$  Debye peak, Fig. 6(c). The broadening of the DCPLs is caused by increased curvature of the path lengths at lower  $\phi_{\text{core}}$  values. The current density plots and overlaid conduction paths, Fig. 6(a) (i)–(iii), are 2D slices extracted from the full 3D dataset. However, the path length statistics were calculated from the 3D model and not just the plots shown in Fig. 6.

#### IV. Discussion

The simulations for the SLM and encased models highlight the significance and relationship between their physical and electrical microstructures, their influence on the impedance spectra produced and the applicability of the encased cubic grain model to assess core–shell volume fraction in ceramics. The SLM results in Figs. 2, 3, and 5 validate our FEM. They show that  $\tau$  is independent of the chosen geometry for all values of  $\phi_{\text{core}}$  for both the core and shell regions. As expected, the magnitude of the current density in the two regions is generally different and frequency dependent. The behavior at  $\phi_{\text{core}} = 0.50$  [Fig. 2(e) (i)] shows high current density in the resistive shell region at low frequency, whereas higher current density occurs in the conductive core region at high frequency, Fig. 2(e) (iii). As  $\tau_{\text{shell}} = 1000 \tau_{\text{core}}$ , the maximum value of  $M''$  for the shell occurs at much lower frequency than for the core and the two responses are well resolved in  $M^*$  plots, Fig. 2(c). The current density is homogeneous within each region, for all values of  $\phi_{\text{core}}$  and frequency, Fig. 2(e) (i)–(iii). For the SLM, this allows reliable extraction of core volume fraction and R, C,  $\tau$  as a function of the input core fraction  $\phi_{\text{core}}$  as shown in Figs. 3(a) and 5, respectively.

The results for the encased model in Figs. 2, 3, and 5 show the problems in extending the BLM to core–shell structures. The most obvious is the dependence of  $\tau_{\text{core}}$  on  $\phi_{\text{core}}$  for a wide range of  $\phi_{\text{core}}$  values (in Fig. 4, for  $\phi_{\text{core}} < 0.8$ , and our chosen values for  $\sigma$  and  $\epsilon_r$ ). When  $\phi_{\text{core}} = 0.50$  (Fig. 2),

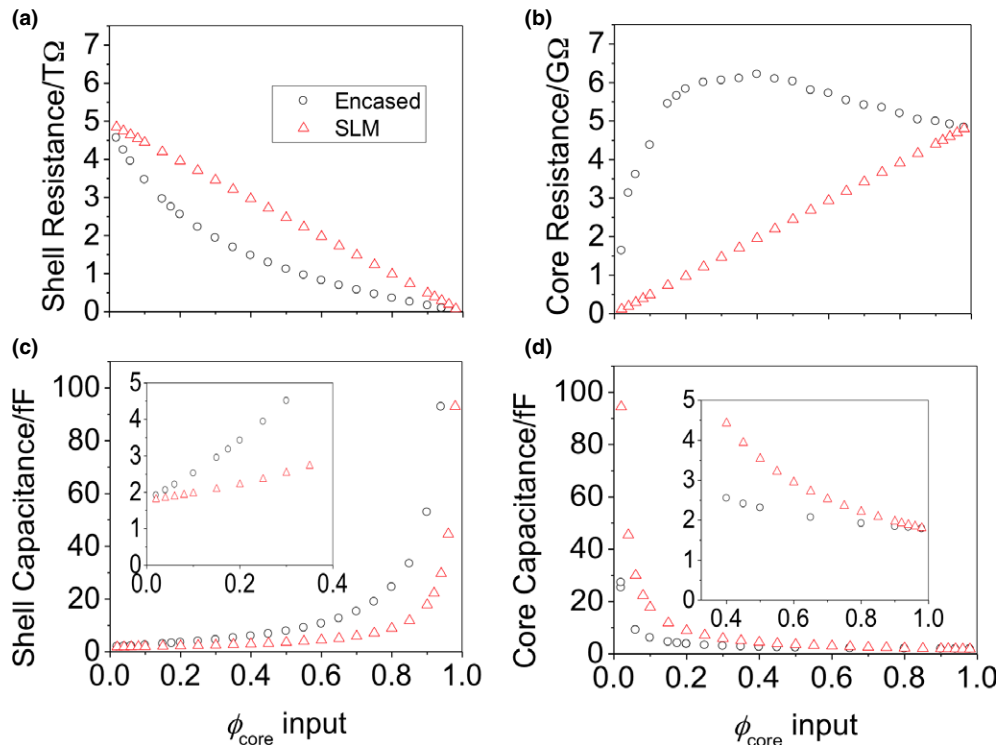


Fig. 5. (a) Extracted shell resistance, (b) core resistance, (c) shell capacitance, and (d) core capacitance for a range of input values of  $\phi_{\text{core}}$  for the SLM and encased models. Inserts in (c) and (d) are an enlargement showing the change in  $\phi_{\text{core}}$  values at lower capacitance.

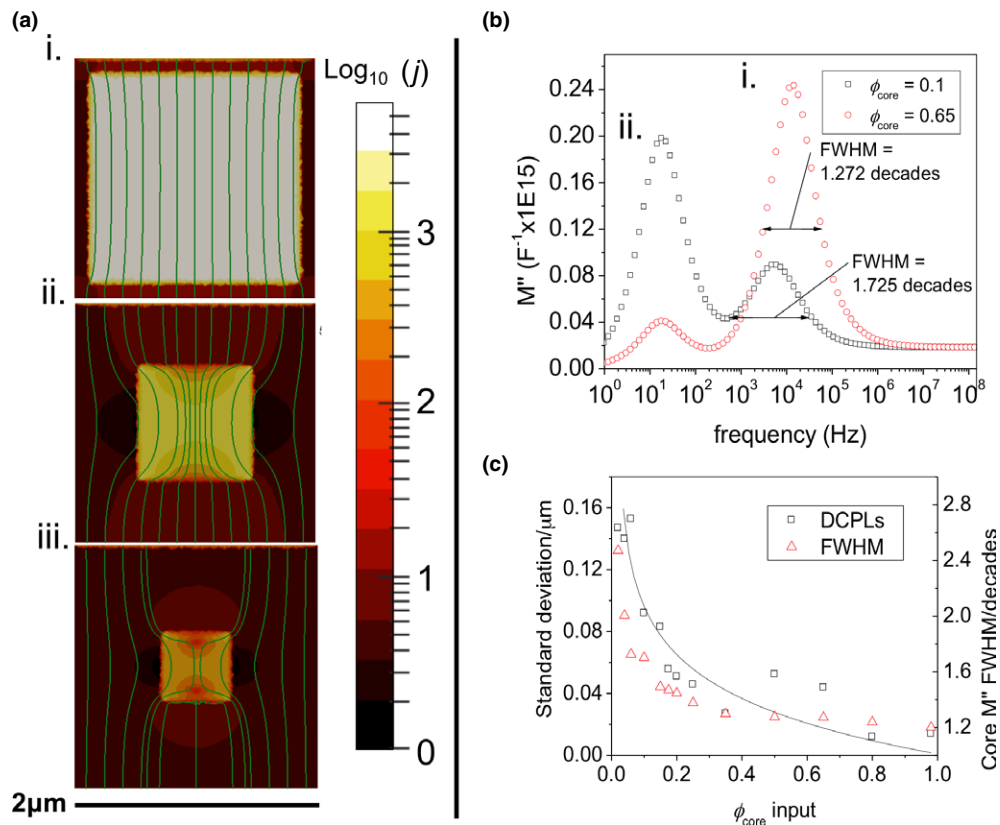


Fig. 6. (a) Current density plots ( $j$  in  $\text{A}/\text{m}^2$ ) for  $\phi_{\text{core}}$  values of 0.65, 0.10, and 0.02 in (i), (ii) and (iii), respectively, with overlaid simulated conduction pathway trajectories in green. The starting points are evenly spaced for (i) and (ii); the starting points have been chosen to show the largest trajectories on (iii). (b)  $M''$  spectroscopic plots for the encased model for a large encased core volume ( $\phi_{\text{core}} = 0.65$ , i) and a small encased core volume ( $\phi_{\text{core}} = 0.1$ , ii); note the increased FWHM of the high-frequency peak for (ii). The peaks for (iii) are not shown as they are poorly resolved. (c) The trend between the standard deviation of the DCPLs and the FWHM (of the high-frequency Debye peak) for a range of  $\phi_{\text{core}}$  input values. The solid line is a guide to the eye for the standard deviation of the path lengths.

the change in physical microstructure from the SLM to the encased model clearly has a dramatic influence on the  $M^*$  response. This is shown by comparing Figs. 2(c) and (d), the volume fractions obtained from the ratios of the  $M^*$  arc diameters and the current density behavior observed [Fig. 2(e)] within the core and shell regions. This has significant consequences for the electrical microstructure of the encased model.

The current density plots in Fig. 2(e) explain the discrepancy between the volume fractions calculated from the simulated IS data in Fig. 2(d) and the input values for the encased model. Although the variation in the current density with frequency is similar in the encased model to the SLM, the current density is no longer homogenous within each region. Figure 2(e) (iv) shows the current to take the path of least resistance when presented with a choice of flowing through the (conductive) core or the (resistive) shell for the encased model. This leads to a lower current density in the shell region parallel to the core, reducing its contribution to the magnitude of the impedance response. This loss of effective thickness in the shell region increases the measured capacitance, which gives a smaller shell (low frequency)  $M^*$  arc diameter in Fig. 2(d). Using Eq. (1) to estimate volume fractions from  $M^*$  arcs therefore underestimates the shell volume fraction and hence overestimates the core as our simulations are performed for a constant grain volume. As the core fraction decreases, the error in the core fraction estimated from  $M^*$  spectra increased to over 250% [in Fig. 3(b) for  $\phi_{\text{core}} = 0.02$ ]. The error in the extracted core fraction exceeds 25% for  $\phi_{\text{core}} < 0.7$ .

Another approach would be to insert extracted capacitance values into the Bonanos–Lilley equations to predict the volume fractions of the regions. This has previously been tried by Kidner *et al.*<sup>13,27</sup> However, this approach still underestimates  $\phi_{\text{core}}$  because the BLM assumes nested cubes, whereas the Bonanos–Lilley equations, being derived from EMT, assumes nested spheres. A cube is more intrinsically conductive than a sphere assuming both shapes are the same material and volume.<sup>28</sup> Any simulations undertaken therefore require the correct physical shape of the microstructure to ensure results obtained from the simulated IS data are relevant and meaningful.

Although the shell region parallel to the core in the encased model has a much lower current density than the rest of the model, it is not zero. Furthermore, with

decreasing  $\phi_{\text{core}}$  the area of the shell region parallel to the core presented to the incoming current increases, reducing its effective resistance. Using the stream trace analysis of the current density vector field we highlight two conduction pathways at low  $\phi_{\text{core}}$ , Fig. 6(a) (i)–(iii). First, there is a long conduction path that curves more strongly toward the core as  $\phi_{\text{core}}$  is reduced. Second, there is a short conduction path that goes straight through the parallel shell phase. A statistical analysis of the conduction path lengths for a range of volume fractions showed that the distribution of the conduction path lengths broadens as  $\phi_{\text{core}}$  decreased. Measuring the FWHM of the high-frequency (core)  $M''$  Debye peak revealed that both the core FWHM and the standard deviation of the distribution of the conduction path lengths increases as  $\phi_{\text{core}}$  decreases, Fig. 6(b). A secondary effect of the increased curvature of the long conduction pathways was the increased heterogeneity of the current density within the core, leading to the unusual conduction behavior and  $R_{\text{core}}$  values shown in Fig. 4, and the dependence of  $\tau_{\text{core}}$  on the geometry, Fig. 5(b).

These unusual core effects can be analyzed by inspecting variations in the electric field experienced by the core and shell regions in both the SLM and encased models. For both models the electrode area and cube volume are fixed for all  $\phi_{\text{core}}$ . In all cases, the current density spreads laterally through the region in series with the electrodes to minimize overall resistance. This is in good agreement with a previous modeling study.<sup>25</sup> For the SLM, the core and shell regions are connected only in series and therefore the electric field remains homogeneous in each region, Fig. 7(a). In this model, the physical and electrical microstructure are identical and any change in the physical microstructure arising from a change in  $\phi_{\text{core}}$  will be reflected in the electrical microstructure and can be readily analyzed using IS data.

Due to the coexistence of series and parallel pathways in the encased model, the electric field experienced by the core region depends on both the physical microstructure (dimensions and morphology) and the material properties of the two phases. In the present model, where the cores are cubes and  $\sigma_{\text{core}} = 1000\sigma_{\text{shell}}$ ;  $\epsilon_{r,\text{core}} = \epsilon_{r,\text{shell}}$ , the electric field experienced by the core changes with  $\phi_{\text{core}}$ . For  $\phi_{\text{core}} \geq 0.65$  the electric field (and current density) experienced by the core is reasonably homogeneous, Fig. 7(b), as the shell region parallel to the core is thin with a high effective resistance. The electrical microstructure therefore remains similar to the

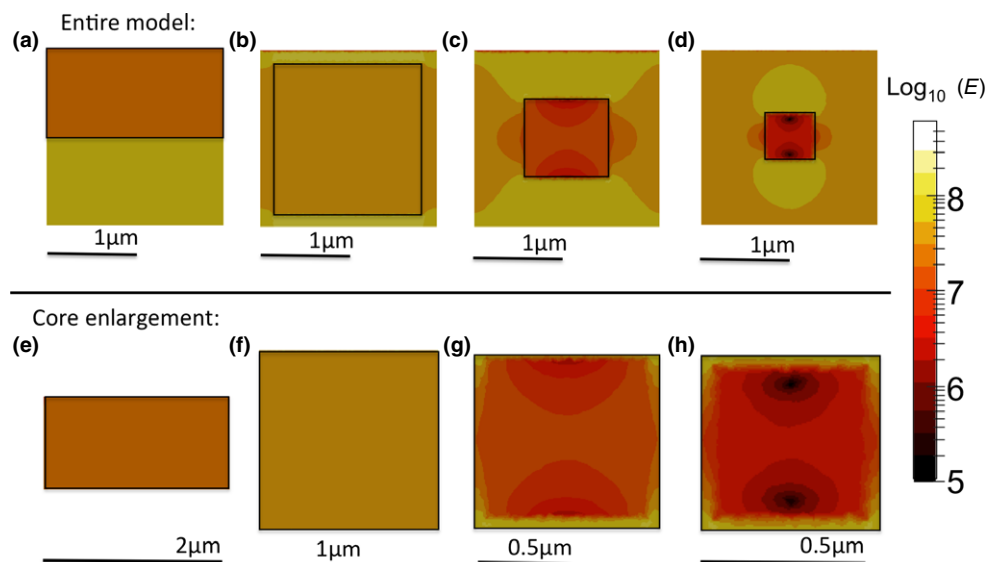


**Fig. 7.** (a) Electric field plots taken at the high-frequency Debye response for: SLM for  $\phi_{\text{core}} = 0.50$ . (b)–(d) Encased models with  $\phi_{\text{core}}$  values of 0.65, 0.1, and 0.02, respectively. (e)–(h) Enlargements of the core field plots [corresponding to regions in (a)–(d) surrounded by black box].  $E$  is the electric field and has units of V/m.

physical microstructure. For lower  $\phi_{\text{core}}$ , the electric field concentrates at the vertices of the cubic core region, generating regions of high and low field inside the core. This is shown in Figs. 7(c) and (d) for  $\phi_{\text{core}} = 0.10$  and 0.02. This effect dramatically alters the electrical microstructure of the core compared to its physical microstructure. In particular, regions of high electric field extend from the cube corners and cube faces perpendicular to the electrode contacts, whereas regions of low electric field are observed near the surface of the cube centers for the cube faces that are parallel to the electrode contacts. This leads to an apparent dependence of  $\tau_{\text{core}}$  on the geometry of the system for  $\phi_{\text{core}} < 0.80$  for our encased model, Fig. 4. However, this will change for different physical microstructures (e.g., spheres as opposed to cubes) and for different material properties of the core and shell regions.

## V. Conclusion

Finite element simulations have shown the electrical microstructure of an encased cubic core-shell microstructure can be significantly different from its physical microstructure. The electrical microstructure is defined by both the electrical properties of the core and shell regions and by how the physical microstructure modifies the electrical field and consequent current pathways in space. Regions of low current density contribute less to the magnitude of the impedance response but if their effective resistance is low enough, additional conduction pathways can form and broaden the  $M''$  Debye peak associated with the core region. A reduction in the impedance response from blocking (resistive shell region) components makes extracting the volume fractions from  $M''$  plots or  $M''$  spectra increasingly unreliable at lower values of the core fraction. At higher  $\phi_{\text{core}}$  values ( $0.7 < \phi_{\text{core}} < 1$ ) it is possible to extract volume fractions with acceptable error bars. For lower  $\phi_{\text{core}}$  values, substantial amounts of current must curl to bypass any surrounding blocking regions and enter the core. This leads to heterogeneous current density within the core region. This effect is increased by a heterogeneous electric field, leading to enhancement of  $\tau_{\text{core}}$ . For the encased model presented here, which was based on an extension of the BLM, it should be noted that the increase in  $\tau_{\text{core}}$  is significant only for  $\phi_{\text{core}} < 0.8$ . This is due to our choice of nested cubes to build a microstructure. This highlights the importance of the physical structure of the grains and core and shell regions when attempting to simulate IS data using FEM. This can have a dramatic effect on the electrical microstructure. Future work is currently underway to; (i) investigate possible modifications to the known analytical equations to account for this effect, and (ii) how the use of more realistic grain shapes, roughness and porosity (i.e., a closer description of a real physical microstructure) influences the electric field and therefore the electrical microstructure and  $\tau$  values of core-shell and related microstructures. The influence of core and shell region material parameters on the IS response can then be explored.

## Acknowledgment

We thank the EPSRC for financial support (EP/G005001/1).

## References

- <sup>1</sup>A. R. West, D. C. Sinclair, and N. Hirose, "Characterization of Electrical Materials, Especially Ferroelectrics, by Impedance Spectroscopy," *J. Electroceram.*, **1** [1] 65–71 (1997).
- <sup>2</sup>B.-Y. Chang and S.-M. Park, "Electrochemical Impedance Spectroscopy," *Annual Annu. Rev. Anal. Chem.*, **3**, 207–29 (2010).
- <sup>3</sup>J. Ho, T. R. Jow, and S. Boggs, "Historical Introduction to Capacitor Technology," *IEEE Elect. Insul. Mag.*, **26** [1] 20–5 (2010).
- <sup>4</sup>AVX Capacitor Specifications, <http://www.avx.com/docs/masterpubs/mccc.pdf> (accessed 1/11/14).
- <sup>5</sup>S.-C. Jeon, B.-K. Yoon, K.-H. Kim, and S.-J. Kang, "Effects of Core/Shell Volumetric Ratio on the Dielectric-Temperature Behavior of BaTiO<sub>3</sub>," *J. Adv. Ceram.*, **3** [1] 76–82 (2014).
- <sup>6</sup>D. C. Sinclair and A. R. West, "Impedance and Modulus Spectroscopy of Semiconducting BaTiO<sub>3</sub> Showing Positive Temperature-Coefficient of Resistance," *J. Appl. Phys.*, **66** [8] 3850–6 (1989).
- <sup>7</sup>P. Fiorenza, R. Lo Nigro, P. Delugas, V. Raineri, A. G. Mould, and D. C. Sinclair, "Direct Imaging of the Core-Shell Effect in Positive Temperature Coefficient of Resistance-BaTiO<sub>3</sub> Ceramics," *Appl. Phys. Lett.*, **95** [14] 142904 (2009).
- <sup>8</sup>D. C. Sinclair, T. B. Adams, F. D. Morrison, and A. R. West, "CaCu<sub>3</sub>Ti<sub>4</sub>O<sub>12</sub>: One-Step Internal Barrier Layer Capacitor," *Appl. Phys. Lett.*, **80** [12] 2153–5 (2002).
- <sup>9</sup>R. Schmidt, M. C. Stennett, N. C. Hyatt, J. Pokorny, J. Prado-Gonjal, M. Li, and D. C. Sinclair, "Effects of Sintering Temperature on the Internal Barrier Layer Capacitor (IBLC) Structure in CaCu<sub>3</sub>Ti<sub>4</sub>O<sub>12</sub> (CCTO) Ceramics," *J. Eur. Ceram. Soc.*, **32** [12] 3313–23 (2012).
- <sup>10</sup>S. I. R. Costa, M. Li, J. R. Frade, and D. C. Sinclair, "Modulus Spectroscopy of CaCu<sub>3</sub>Ti<sub>4</sub>O<sub>12</sub> Ceramics: Clues to the Internal Barrier Layer Capacitance Mechanism," *RSC Adv.*, **3** [19] 7030–6 (2013).
- <sup>11</sup>N. Bonanos and E. Lilley, "Conductivity Relaxations in Single-Crystals of Sodium-Chloride Containing Suzuki Phase Precipitates," *J. Phys. Chem. Solids*, **42** [10] 943–52 (1981).
- <sup>12</sup>J. E. Bauerle, "Study of Solid Electrolyte Polarization by a Complex Admittance Method," *J. Phys. Chem. Solids*, **30** [12] 2657–70 (1969).
- <sup>13</sup>N. J. Kidner, N. H. Perry, T. O. Mason, and E. J. Garboczi, "The Brick Layer Model Revisited: Introducing the Nano-Grain Composite Model," *J. Am. Ceram. Soc.*, **91** [6] 1733–46 (2008).
- <sup>14</sup>D. S. McLachlan, M. Blaszkiewicz, and R. E. Newnham, "Electrical Resistivity of Composites," *J. Am. Ceram. Soc.*, **73** [8] 2187–203 (1990).
- <sup>15</sup>J. S. Dean, J. H. Harding, and D. C. Sinclair, "Simulation of Impedance Spectra for a Full Three-Dimensional Ceramic Microstructure Using a Finite Element Model," *J. Am. Ceram. Soc.*, **97** [3] 885–91 (2014).
- <sup>16</sup>J. C. Maxwell, *A Treatise on Electricity and Magnetism*. Clarendon Press, Oxford, 1881.
- <sup>17</sup>J. Fleig and J. Maier, "Finite Element Calculations of Impedance Effects at Point Contacts," *Electrochim. Acta*, **41** [7–8] 1003–9 (1996).
- <sup>18</sup>J. Fleig and J. Maier, "The Influence of Laterally Inhomogeneous Contacts on the Impedance of Solid Materials: A Three-Dimensional Finite-Element Study," *J. Electroceram.*, **1** [1] 73–89 (1997).
- <sup>19</sup>M. Tanemura, T. Ogawa, and N. Ogita, "A New Algorithm for 3-Dimensional Voronoi Tessellation," *J. Comput. Phys.*, **51** [2] 191–207 (1983).
- <sup>20</sup>C. Geuzaine and J.-F. Remacle, "Gmsh: A 3-D Finite Element Mesh Generator with Built-in Pre- and Post-Processing Facilities," *Int. J. Numer. Meth. Eng.*, **79** [11] 1309–31 (2009).
- <sup>21</sup>Scribner Home Page. <http://www.scribner.com/> (accessed 10/10/14).
- <sup>22</sup>A. Henderson, J. Ahrens, and C. Law, *The ParaView Guide*. Kitware Inc, Clifton Park, NY, 2004.
- <sup>23</sup>ParaView Home Page <http://www.paraview.org/> (accessed 06/11/14).
- <sup>24</sup>D. C. Sinclair, "Characterization of Electro-Materials Using ac Impedance Spectroscopy," *Bol. Soc. Esp. Ceram. Vidrio*, **34** [2] 55–65 (1995).
- <sup>25</sup>J. Fleig, S. Rodewald, and J. Maier, "Microcontact Impedance Measurements of Individual Highly Resistive Grain Boundaries: General Aspects and Application to Acceptor-Doped SrTiO<sub>3</sub>," *J. Appl. Phys.*, **87** [5] 2372–81 (2000).
- <sup>26</sup>J. Fleig, "The Grain Boundary Impedance of Random Microstructures: Numerical Simulations and Implications for the Analysis of Experimental Data," *Solid State Ionics*, **150** [1–2] 181–93 (2002).
- <sup>27</sup>N. J. Kidner, Z. J. Homrighaus, B. J. Ingram, T. O. Mason, and E. J. Garboczi, "Impedance/Dielectric Spectroscopy of Electroceramics - Part 2: Grain Shape Effects and Local Properties of Polycrystalline Ceramics," *J. Electroceram.*, **14** [3] 293–301 (2005).
- <sup>28</sup>M. L. Mansfield, J. F. Douglas, and E. J. Garboczi, "Intrinsic Viscosity and the Electrical Polarizability of Arbitrarily Shaped Objects," *Phys. Rev. E: Stat., Nonlinear, Soft Matter Phys.*, **64** [6] 61401–16 (2001). □